To the Graduate Council:

I am submitting herewith a thesis written by Lawrence P. Talley entitled "Radar Cross Section of the Low Flying Aerial Target in B-Band." I recommend that it be accepted in partial fulfillment of the requirements for the degree of Master of Science, with a major in Electrical Engineering.

P. Z. Peebles, Jr.

P. Z. Peebles, Jr., Major Professor

We have read this thesis
and recommend its acceptance:

JC Fung

J. D. Tillman

Accepted for the Council:

L. Evans Roth

Vice Chancellor
Graduate Studies and Research

RADAR CROSS SECTION OF THE LOW FLYING AERIAL TARGET IN B-BAND

A Thesis

Presented for the

Master of Science

Degree

The University of Tennessee, Knoxville

Lawrence P. Talley

December 1979

ABSTRACT

This study presents a methodical determination of a model to analytically estimate the radar cross section (RCS) of the Low Flying Aerial Target (LOFAT) at a frequency of 430 megahertz (MHz). This report approached the problem utilizing approximate theoretical techniques and laboratory RCS measurements of the LOFAT to develop the representative model. Simple shapes, including cylinders, thin wires, a flat circular disk, and a flat rectangular plate were employed to construct the composite model.

The model developed in this study generally exhibited an agreement between measured and calculated RCS of ± 5 dB and within ± 2 dB in the regions from 0° to 20°, 80° to 130°, and 150° to 180°. The model developed will help to satisfy the goal of the Navy to accurately predict the RCS of the LOFAT at frequencies in the B-Band.

TABLE OF CONTENTS

LIST OF FIGURES

CHAPTER I

INTRODUCTION

This report presents an investigation of the radar cross section (RCS) of a Low Flying Aerial Target (LOFAT) (Figure 1.1) at a frequency of 430 megahertz (MHz). The LOFAT is used by the Navy for point weapon evaluation, gunner training, and as a reference target for detection by surveillance radars. The target has been designed to exhibit a minimum RCS of .5 square meter in the forward area at X-Band frequencies. Little is known about the target's RCS at lower frequencies, thus the objective of this paper.

RCS of an object is defined as the 4 times the ratio of the backscattered power per unit solid angle to the incident power per unit area. RCS has units of area denoted by σ (m^2) or units of decibels σ (dBsm) referenced to the backscatter from a one square meter object. RCS can be expressed as follows (1, p. 40)

$$\sigma = \lim_{R \to \infty} 4\pi R^2 \left| \frac{E_r}{E_i} \right|^2 \tag{1.1}$$

E_i is the magnitude of the incident electric field, E_r is the magnitude of the backscattered field, and R is the range from the object to the point of observation. RCS of the object can theoretically be determined by employing exact or approximate techniques. Exact

FIGURE 1.1

LOW FLYING AERIAL TARGET

techniques are generally very difficult to employ, since the scattering problem must usually be solved in the coordinate system of the object; i.e., spherical coordinates for a sphere, cylindrical coordinates for a cylinder, etc. Therefore, exact solutions are known only for simple shapes. Approximate techniques are known in the literature for many objects and accurate numerical results have been demonstrated. This paper will pursue only the approximate techniques. A few of these techniques are as follows:

1. Physical Optics
2. Geometrical Theory of Diffraction
3. Creeping Wave Analysis

To apply the physical optics method to calculate the RCS of an object, the body must be assumed to be a perfect electrical conductor. Physical optics theory describes the behavior of light as it strikes the object. This theory assumes that the backscatter is due solely from specular returns; i.e., returns from the object at angles of reflection relative to the observation point which is equal to the incident angle. The RCS is determined by a plane wave striking the surface of the object and the reflected wave obeying physical optics theory passing through an area of intercept of a body with a plane perpendicular to the incoming wave. Physical optics RCS of an object can be obtained from the following expression (2, p. 123)

$$\sigma = \frac{4\pi}{\lambda^2} \left| \int e^{2ik\rho} \frac{\partial A}{\partial \rho} d\rho \right|^2 \tag{1.2}$$

where λ is the wave length, K is the wave number, A is the area of intercept of a body, and ρ is the coordinate along the radar line of sight. The equation for physical optics sometimes gives poor results, since it does not account for polarization effects or effects from diffraction or creeping wave propagaton into the shadow area of the object.

Geometrical theory of diffraction was primarily developed by Keller (3, pp. 116-130). Geometrical diffraction extends the physical optics theory to account for diffracted rays. Diffracted waves are generated by rays that hit edges, corners, or grazing surfaces. This theory assumes localization of the scattering rays at a point of diffraction and assigns a phase proportional to the optical length of the ray from some reference. Then, based on known problems, a diffraction coefficient is assigned to each diffraction point (scattering center).

Creeping wave theory accounts for waves that pass into the shadow region of an object. This theory is used for small objects that lie in the resonance region. The creeping wave contribution is generally calculated by applying diffraction and decay coefficients obtained from geometrical theory of diffraction.

This paper presents an analysis of theoretical RCS determinations based on applying physical optics techniques. Approximations for the RCS of simple shapes (thin wires, flat plates, cylinders, etc.) will be used in modeling components of the LOFAT.

CHAPTER II

PURPOSE

The aim of this paper is to utilize the results of the laboratory radar cross section (RCS) measurements conducted at the Pacific Missile Test Center on the Low Flying Aerial Target (LOFAT) at a frequency of 430 megahertz (MHz) as a basis in the development of a model that can be used to theoretically determine the LOFAT's RCS. The model was developed by utilizing the physical optics techniques. This study will help satisfy a desire of the Navy to be able to predict the RCS of the LOFAT at lower frequencies for all target azimuth aspects and zero degree elevation aspect.

CHAPTER III

LOW FLYING AERIAL TARGET

DESCRIPTION

The Low Flying Aerial Target (LOFAT) is 3.07 meters long and .76 meters in diameter. The basic airframe consists of a nose and tail assembly that are molded into a one piece structure using molded fiberglass and rigid polyurethane foam. Molded within the nose and tail assemblies is a centrally located aluminum tube approximately 15 centimeters in diameter that serves as a strongback for the assembled airframe and an attachment point for the four fins, tow-bar, forward skid assembly, nose-tip, and witness plate. The forward skid assembly is fabricated from aluminum tubing with steel skids and is attached to a cast iron nose-tip. The four fins are fabricated from plywood and are attached to the tube by eight aluminum supports. The witness plate is .76 meters in diameter fabricated from aluminum and is positioned at the midsection of the LOFAT's airframe.

CHAPTER IV

LABORATORY METHODS AND PROCEDURES

Measurement System and Technique

The laboratory radar cross section (RCS) measurements (4) of the Low Flying Aerial Target (LOFAT) were conducted in the Pacific Missile Test Center microwave anechoic chamber. The chamber is designed to provide an electromagnetic environment approximately that of free space at microwave frequencies. The LOFAT was positioned on a small vertical styrofoam column extending halfway to the ceiling near one end of the chamber. The measurement equipment was located at the same level approximately 22 meters from the target.

The measurement signal was generated by a stable radio-frequency source, and was radiated by a transmitting antenna which provided target illumination with field density variations of less than 1 decibel (dB). The backscattered signal was detected and recorded. In the absence of a target, a residual signal from chamber wall reflections and from crosstalk between antennas is received. This residual signal was cancelled, and the system was calibrated in terms of absolute RCS by measuring the backscattered signal from a precision metal sphere 71 centimeters in diameter. Following cancellation and calibration, the target was positioned on the styrofoam column. Data were acquired as the column was rotated through a complete revolution.

Data Acquisition

The RCS measurements were digitally recorded on magnetic tape by a data acquisition system. The recording system allows a resolution of 0.1 dB, an accuracy of ±0.1 dB, and a dynamic range of 80 dB. The LOFAT data were sampled at 0.04-degree intervals.

Data Processing

Since RCS of objects exhibit large erratic fluctuations as a function of aspect angle, the data were converted to logarithmic form. Because the RCS is proportional to the backscatter signal power, the RCS was expressed in terms of decibels relative to one square meter by the expression

$$\sigma\,(\mathrm{dBsm}) = 10 \log \sigma\,(\mathrm{m}^2) \tag{4.1}$$

The large complex fluctuations, caused by interference among the backscattered signals from the various contributors of the LOFAT, preclude a concise quantitative description of the RCS. Therefore, the data were treated statistically.

The technique for smoothing fluctuations in the raw data consisted of determining the cumulative probability distribution of the data contained in a small angular sector and plotting the fiftieth percentile as a function of aspect angle. The fiftieth percentile, median value, represents the value of RCS that exceeds 50 percent of the data samples within the prescribed angular interval. The data were processed by computing the percentiles of the RCS resulting from aspect variations that were normally distributed with a standard deviation of 2 degrees. The computations were then repeated at 1 degree aspect angle intervals.

CHAPTER V

THEORETICAL METHOD

Modeling

When attempting to determine the radar cross section (RCS) of a complex shape, the first consideration is modeling. In many instances, the object is much larger than the wave length being considered, so modeling the object by an equivalent spheroid is usually sufficient. This is usually the exception, and modeling of complex shapes can become quite involved. The technique presented in this study is to segment the Low Flying Aerial Target (LOFAT) geometry into an ensemble of simple geometric shapes.
It was further assumed that the creeping wave and traveling wave phenomena effects were negligible. The geometrical model developed for the LOFAT (Figure 5.1) consists of two cylinders, a disk, a plate and three thin wires. The cylinders represent the structural aluminum tube that runs the entire length of the LOFAT. The disk represents the witness plate, the plate represents the fin supports, and the thin wires represent the front strut assembly and the wire cable that serves as the connecting strut for the fins.

Calculations

Cylinder. The expression chosen to represent the RCS of the cylinders is (5, P. 842)

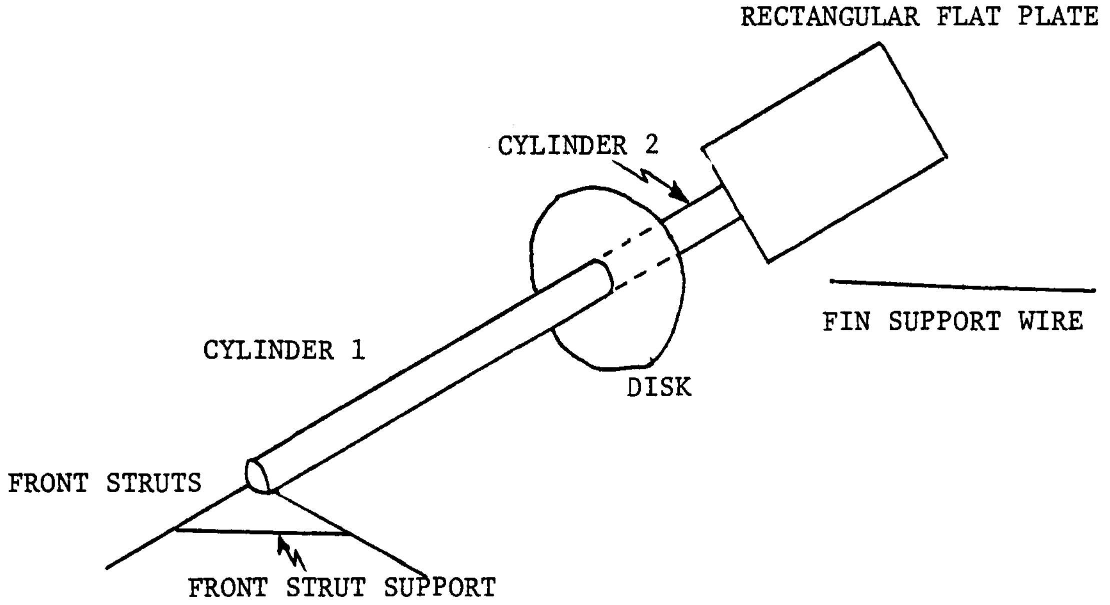

FIGURE 5.1

COMPOSITE LOW FLYING AERIAL TARGET MODEL

$$\sigma = \pi a^2 \sin^2\theta \left(\frac{\sin(KL \cos\theta)}{\cos\theta} \right)^2 (A^2 + B^2) \qquad (5.1)$$

where $A = J_1 (2Ka \sin\theta)$, $B = 2/\pi - S_1 (2Ka \sin\theta)$, a is the cylinder radius, θ is the angle between the cylinder axis and the direction of incidence, L is the length of the cylinder and K is the wave number. J_1 is the Bessel function of the first order and S_1 is the Struve function of the first order. Expression (5.1) yields good results when the cylinder's dimensions are large in comparison to the wave length. Expressions 5.2 and 5.3 were used to determine the values of the Bessel and Struve functions as a function of aspect.

$$J_1(x) = \sum_{n=0}^{\infty} \frac{(-1)^n}{n!(n+1)!} \left(\frac{x}{2}\right)^{2n+1} \qquad (5.2)$$

$$S_1(x) = \left(\frac{x}{2}\right)^2 \sum_{n=0}^{\infty} \frac{(-1)^2 \left(\frac{x}{2}\right)^{2n}}{\Gamma(n+3/2)\,\Gamma(n+5/2)} \qquad (5.3)$$

Wire. The RCS of a thin wire whose radius is small compared to wave length and length is long compared to the wave length can be accurately determined by using Chu's expression (5, p. 842)

$$\sigma = \frac{\pi L^2 \sin^2\theta \left(\dfrac{\sin\left(\dfrac{2\pi L}{\lambda} \cos\theta\right)}{\dfrac{2\pi L}{\lambda} \cos\theta} \right)^2}{\left(\dfrac{\pi}{2}\right)^2 + \left(\ln \left(\dfrac{\lambda}{1.78\, \pi a \sin\theta} \right) \right)^2} \cos^4 \phi \qquad (5.4)$$

where λ is the wave length, L is the length of the wire, a is the radius of the wire, θ is the angle between the wire axis and the direction of incidence and ϕ is the angle between the polarization direction and the plane formed by the wire and the direction of incidence. It should be noted that Chu's formula is based on a methodology assuming the wire's radius is 1/900 of its length, although the expression can be applied to a wide range of radius values.

Disk. The expression employed to determine the RCS of the circular flat plate is (5, p. 844)

$$\sigma = \frac{\pi a^2}{\tan^2\theta} \left(J_1 (2 K a \sin\theta) \right)^2 \qquad (5.5)$$

where a is the radius of the disk, J_1 is the Bessel function of the first order, θ is the angle between the disk axis and the direction of incidence, and K is the wave number. Expression 5.5 yields a good approximation of the RCS of a disk when $Ka \gg 1$.

In cases where $Ka \approx 1$ or slightly larger, the solution will provide a measure of central tendency.

Rectangular Flat Plate. Applying the physical optics method to the determination of the RCS of a rectangular flat plate the following expression is obtained (2, p. 123)

$$\sigma = \frac{4\pi W^2 L^2}{\lambda^2} \frac{\sin^2\theta \ \sin^2(KL\cos\theta)}{(KL\cos\theta)^2} \tag{5.6}$$

where W is the width of the plate, L is the length of the plate, λ is the wave length, θ is the angle between the rectangular flat plate and the direction of incidence, and K is the wave number. This expression will agree very well with measured data when the plate's characteristic dimensions are large when compared to wave length.

Combining the Component Contributors

The next step in the process to determine the LOFAT RCS was to resolve the problem of combining all the contributors. The first step in this process was to determine shadowing effects. Based on physical optics theory, only the parts of the LOFAT that contribute to the RCS are those parts having specular reflections, thus the parts in the shadow of another will not contribute significantly to the LOFAT RCS. Components that were shadowed but whose reflections were 20 dB below that of the major contributors were not considered critical components, and shadowing compensations were not performed.

Next, an expression was needed to describe the composite model that would show the RCS peaks and nulls as a function of aspect angle (angle of incidence). This was realized from the following expression (6, p. 108)

$$\sigma_T = \left| \sum_{K=1}^{N} \sqrt{\sigma_K} \; \exp i \phi_K \right|^2 \tag{5.7}$$

where σ_T = RCS by relative phase, σ_K = RCS of the Kth contributor, and ϕ_k = relative phase angle associated with the Kth contributor. The magnitudes of ϕ_k were determined by selecting the reference plane normal to the direction of incidence centered at the disk and determining the distances from this reference plane to the various contributors for a particular aspect angle. The following expression represents the magnitude of ϕ_k (6, p. 109)

$$\phi_K = \frac{4\pi d}{\lambda} \tag{5.8}$$

where d is the distance from the reference plane to the point scatters, and λ is the wave length. Utilizing this technique, the LOFAT RCS expression (5.9) was determined by combining all the various scatters using equations (5.7) and (5.8)

$$\sigma_T = \Big| \sqrt{\sigma_1}\, e^{i\phi_1} + \sqrt{\sigma_2}\, e^{i\phi_2} + \sqrt{\sigma_2}\, e^{i\phi_3} + \sqrt{\sigma_3}\, e^{i\phi_4} + \sqrt{\sigma_4}\, e^{i\phi_5} + \sqrt{\sigma_5}\, e^{i\phi_6} + \sqrt{\sigma_6}\, e^{i\phi_7} + \sqrt{\sigma_7}\, e^{i\phi_8} \Big|^2 \qquad (5.9)$$

Parameters in this expression are defined in Table 5.1.

TABLE 5.1

PARAMETER DEFINITIONS FOR EXPRESSION 5.9

PARAMETER	COMPONENT	RADAR CROSS SECTION EXPRESSION
σ_1, ϕ_1	Disk	5.5
σ_2, ϕ_2, ϕ_3	Front Struts	5.4
σ_3, ϕ_4	Cylinder 1	5.1
σ_4, ϕ_5	Rectangular Flat Plate	5.6
σ_5, ϕ_6	Cylinder 2	5.1
σ_6, ϕ_7	Front Strut Support	5.4
σ_7, ϕ_8	Fin Support Wire	5.4

CHAPTER VI

RESULTS AND DISCUSSION

Utilizing expression 5.9 the component radar cross sections (RCS's) were assembled to develop the model to describe the Low Flying Aerial Target (LOFAT) RCS in B-Band. Since the LOFAT is a complex shape and the methods employed to describe each component RCS were approximations, expression 5.9 was not totally adequate to predict the RCS of the LOFAT in B-Band. Therefore, adjustments, based on measured data, to some of the individual component RCS magnitudes and dimensions were necessary to obtain the desired model. These adjustments were empirically determined. A rigorous mathematical model was not pursued. The results of this analysis are presented in Figure 6.1 along with the measured data. Figure 6.2 shows the results of the composite model without the magnitude and dimension adjustments applied to various components. The results clearly indicate that the model without any adjustments did not adequately represent the RCS of the LOFAT. All the data points plotted from the model were processed by averaging the data over $\pm 2^{\circ}$ intervals about the particular aspect of interest. These computations were repeated in 1 degree increments. This technique was employed to match the technique used to statistically generate the measured data. The results show that agreement between measured and calculated results were generally

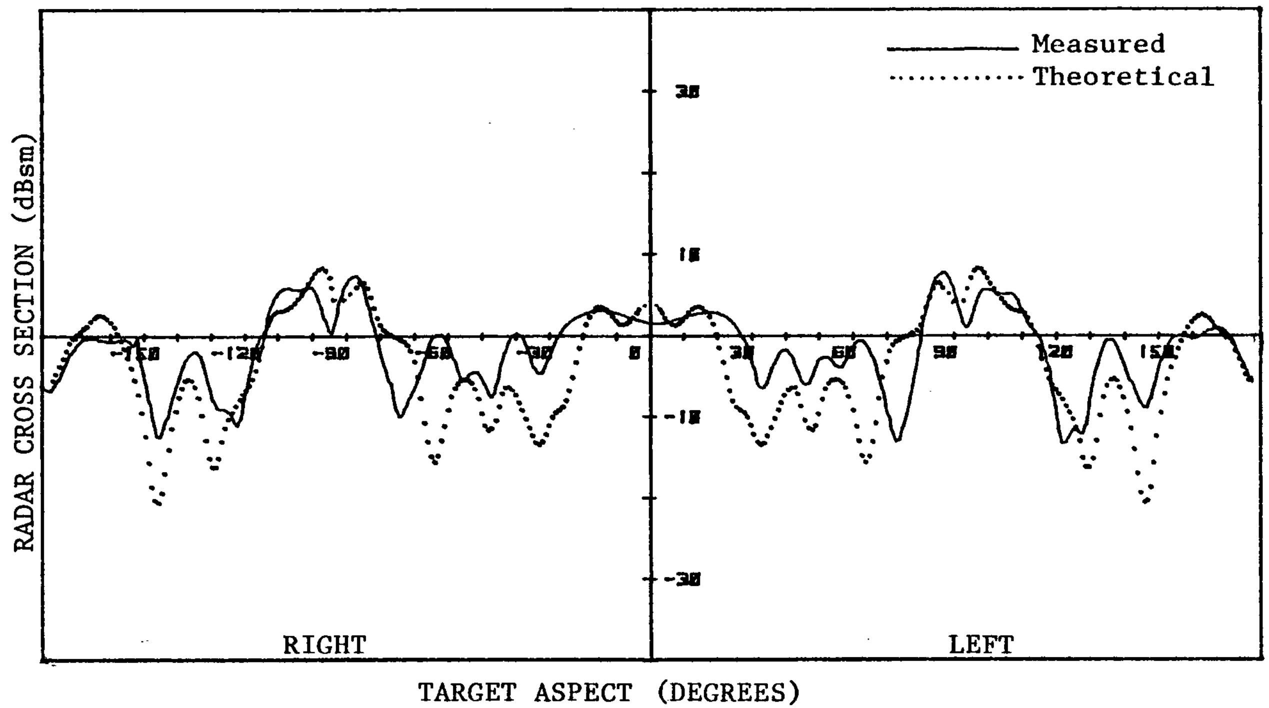

FIGURE 6.1

RADAR CROSS SECTION OF LOW FLYING AERIAL TARGET

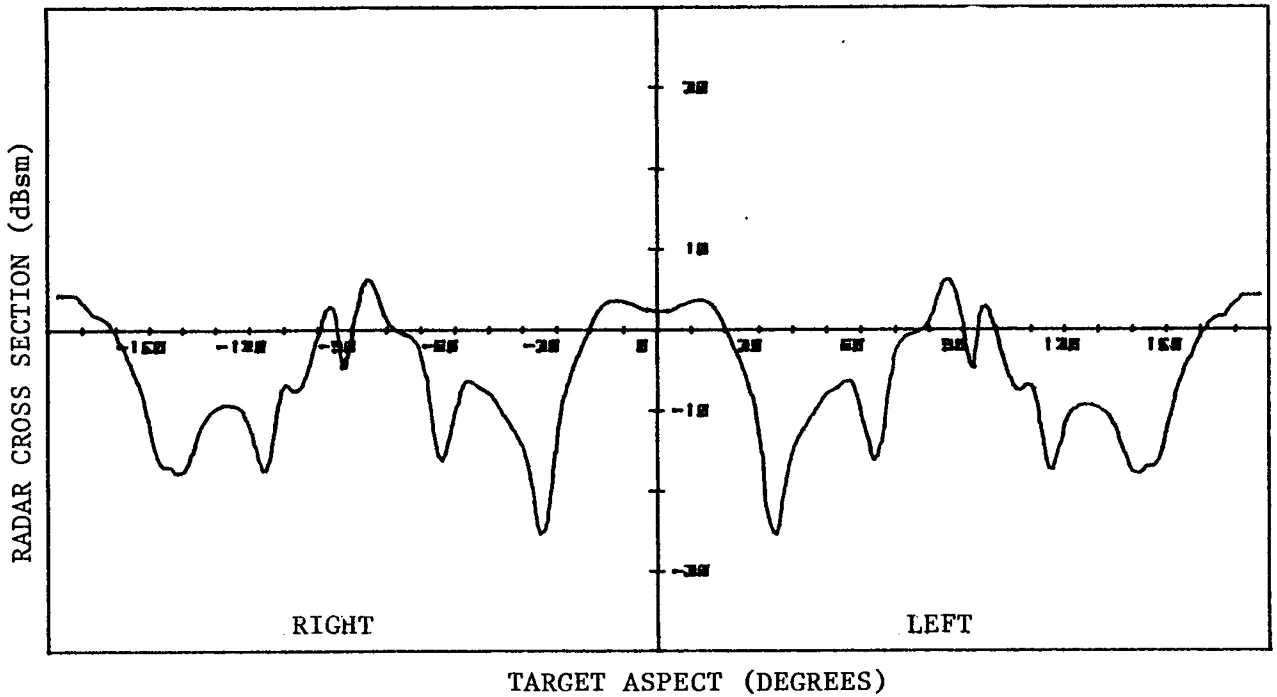

FIGURE 6.2

THEORETICAL RADAR CROSS SECTION OF THE LOW FLYING AERIAL TARGET
PRIOR TO EMPIRICAL ADJUSTMENTS

within ± 5 dB, except in the regions from 20° to 35°, 60° to 80° and 140° to 150°. Agreement between measured and calculated RCS within ± 2 dB was obtained in the regions from 0° to 20°, 80° to 130° and 150° to 180°. Table 6.1 depicts the component dimensions, phase relationships, shaded regions, and magnitude factors utilized to generate the final model.

Table 6.1 shows that the two front strut component RCS magnitudes (expression 5.4) were multiplied by a factor of 64/3 to adequately represent the measured data in the forward region. A much better data match at all aspects and clearly defined nulls and peaks in the 30° to 60° aspect region were achieved by applying the adjustment factor to expression 5.4. This phenomena may be attributed to two factors. First, expression 5.4 was formulated for a wire whose ratio of radius to length was 900, while the ratio of radius to length of the strut was 32. Even though expression 5.4 has proven to be accurate over a wide range of radii, some variation from the expected RCS estimate can be expected for such a large difference. Second, some power gain can be expected from the struts. The physical structure resembles a multi-element antenna. Since the analysis of this structure is beyond the scope of this paper, the RCS was mathematically approximated by employing expression 5.4 and emperically adjusting the RCS magnitude of the struts to match the measured data. Figure 6.3 presents the RCS of each front strut component. The wave shape is not uniform due to shadowing effects in the 90° to 180° region.

TABLE 6.1

LOW FLYING AERIAL TARGET MODEL PARAMETER DATA

COMPONENT	DIMENSION	RCS EXPRESSION	PHASE RELATIONSHIP	ASPECT REGION
Disk	Radius=.38m	σ_1	$\phi_1=0$	$0^\circ<\theta<140^\circ$
				$170^\circ<\theta\le 180^\circ$
		$.7\sigma_1$		$140^\circ<\theta\le 170^\circ$
Front Struts	Radius=.022m	$64/3\sigma_2$	$\phi_2=-1.58 \sin(79^\circ+\theta)$	$0^\circ<\theta\le 11^\circ$
	Length=.686m		$\phi_2=-1.58 \sin(\theta+79^\circ)$	$11^\circ<\theta\le 90^\circ$
			$\phi_3=-1.58 \sin(79^\circ-\theta)$	$0^\circ<\theta<79^\circ$
			$\phi_3=1.58 \sin(\theta-79^\circ)$	$79^\circ<\theta\le 90^\circ$
	Radius=.022m		$\phi_2=1.56 \sin(\theta-83^\circ)$	$90^\circ<\theta\le 173^\circ$
	Length=.34m		$\phi_2=1.56 \sin(\theta-173^\circ)$	$173^\circ<\theta<180^\circ$
			$\phi_3=-1.56 \sin(97^\circ-\theta)$	$90^\circ<\theta<97^\circ$
			$\phi_3=1.56 \sin(\theta-97^\circ)$	$97^\circ<\theta\le 180^\circ$
Cylinder 1	Radius=.0762m	σ_3	$\phi_4=-.8 \cos\theta$	$0^\circ<\theta\le 90^\circ$
	Length=1.6m			
	Radius=.0762m		$\phi_4=-(.8+.19 \tan(\theta-90^\circ)$	$90^\circ<\theta<166^\circ$
	Length=1.6-.38 tan $(\theta-90^\circ)$m	Shaded	$(\cos\theta)$	$166^\circ<\theta\le 180^\circ$
Rectangular	Length=.84m	σ_4	$\phi_5=.8 \sin(52^\circ-\theta)$	$0^\circ<\theta\le 52^\circ$
Flat Plate	Width=.359m		$\phi_5=-.8 \sin(\theta-52^\circ)$	$52^\circ<\theta\le 90^\circ$
	Length=.6m	$6\sigma_4$	$\phi_5=-.8 \sin(\theta-52^\circ)$	$90^\circ<\theta\le 142^\circ$
	Width=.359m		$\phi_5=-.8 \cos(\theta-142^\circ)$	$142^\circ<\theta\le 180^\circ$
Cylinder 2	Radius=.0762 m	Shaded		$\theta<28^\circ$
	Length=.61-.32/tan θ m	σ_5	$\phi_6=(.31+.15/\tan\theta) \cos\theta$	$28^\circ<\theta<90^\circ$
	Radius=.0762m		$\phi_6=.3 \cos\theta$	$90^\circ<\theta\le 180^\circ$
	Length=.6m			
Front Strut	Radius=.00318m	$8/3\sigma_6$	$\phi_7=-1.55 \cos\theta$	$0^\circ<\theta\le 90^\circ$
Support	Length=.762m	Shaded		$90^\circ<\theta\le 180^\circ$
Fin Support	Radius=.00483m	$8/3\sigma_7$	$\phi_8=1.15 \cos\theta$	$0^\circ<\theta\le 90^\circ$
Wire	Length=.914m		$\phi_8=1.19 \cos\theta$	$90^\circ<\theta\le 180^\circ$

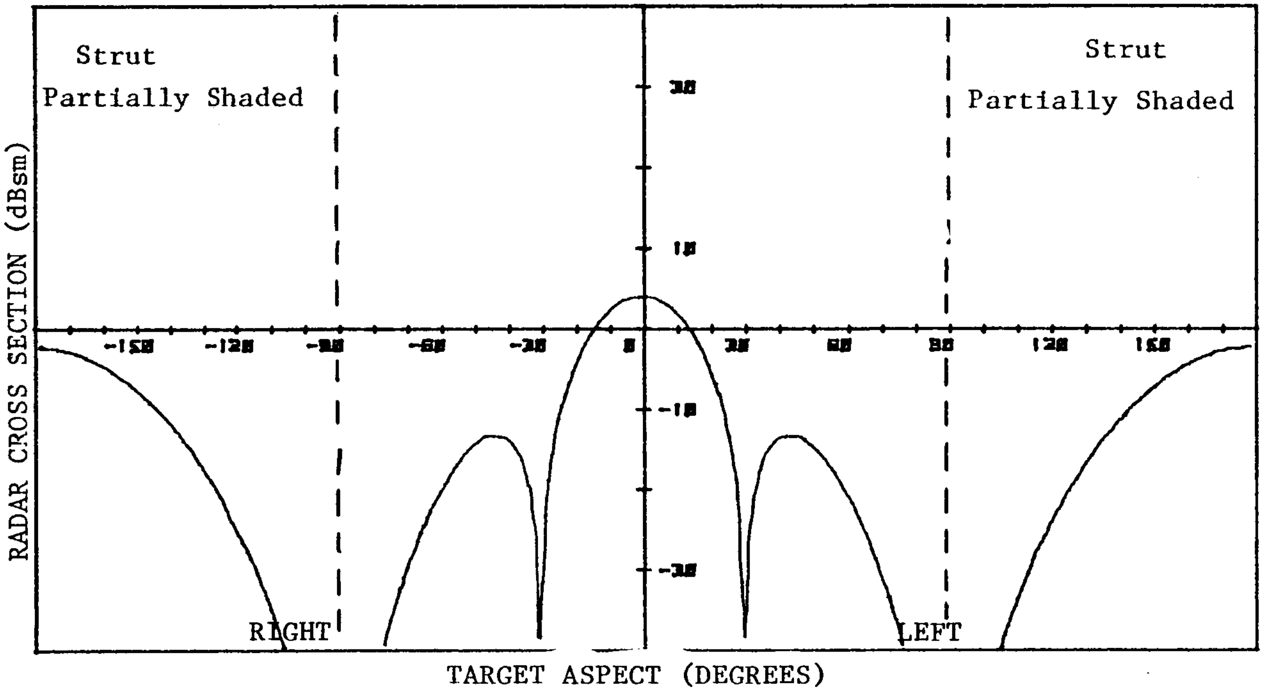

FIGURE 6.3

FRONT STRUT RADAR CROSS SECTION

Analysis of the measured data and individual components in the broadside region revealed that the fin supports were not simple plate reflectors, but formed a 90° corner reflector which exhibited different effects when viewed from different aspects. In the 0° to 90° region the fin supports were best modeled by a flat plate with a length of .84 meters and a width of .359 meters. Its phase center was positioned .49 meters perpendicular from the axis of symmetry of cylinder 2 to compensate for the time delay of the doubly reflected wave. In the 90° to 180° region the length was shortened to .6 meters and the plate's RCS was multiplied by a factor of 6 to match the peaks, nulls and magnitude of the measured data. The same phase center was employed as in the 0° to 90° region. Figure 6.4 presents the RCS contribution of the fin supports. The discontinuity at 90° and non-uniform wave shape are a result of the adjustments made to the plate's length and magnitude from actual in the 90° to 180° region.

Likewise, the fin support wire and front strut support component RCS magnitudes were multiplied by 8/3 to match the measured data. Their contribution to the composite model are presented in Figure 6.5 and Figure 6.6, respectively.

The expressions previously presented in Chapter V (pp. 10-14) to describe the RCS of cylinder 1 (Figure 6.7), cylinder 2 (Figure 6.8) and the disk (Figure 6.9) were only mathematically changed to reflect shadowing effects.

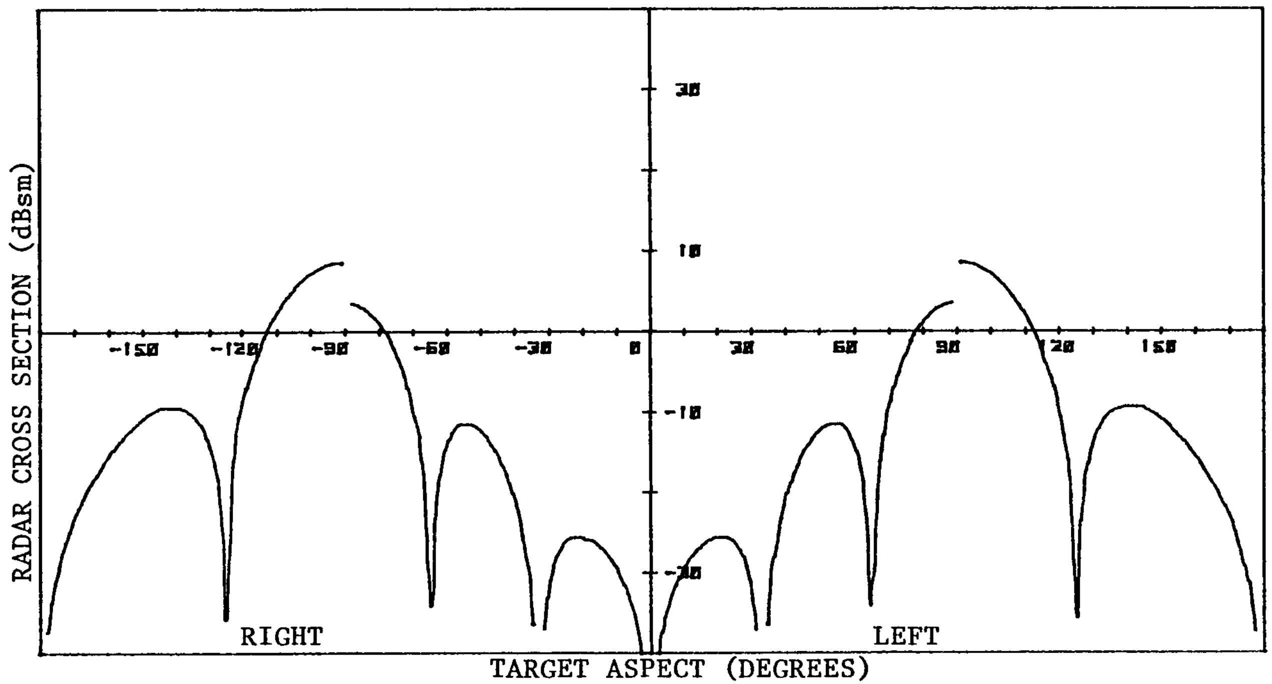

FIGURE 6.4

RECTANGULAR FLAT PLATE RADAR CROSS SECTION

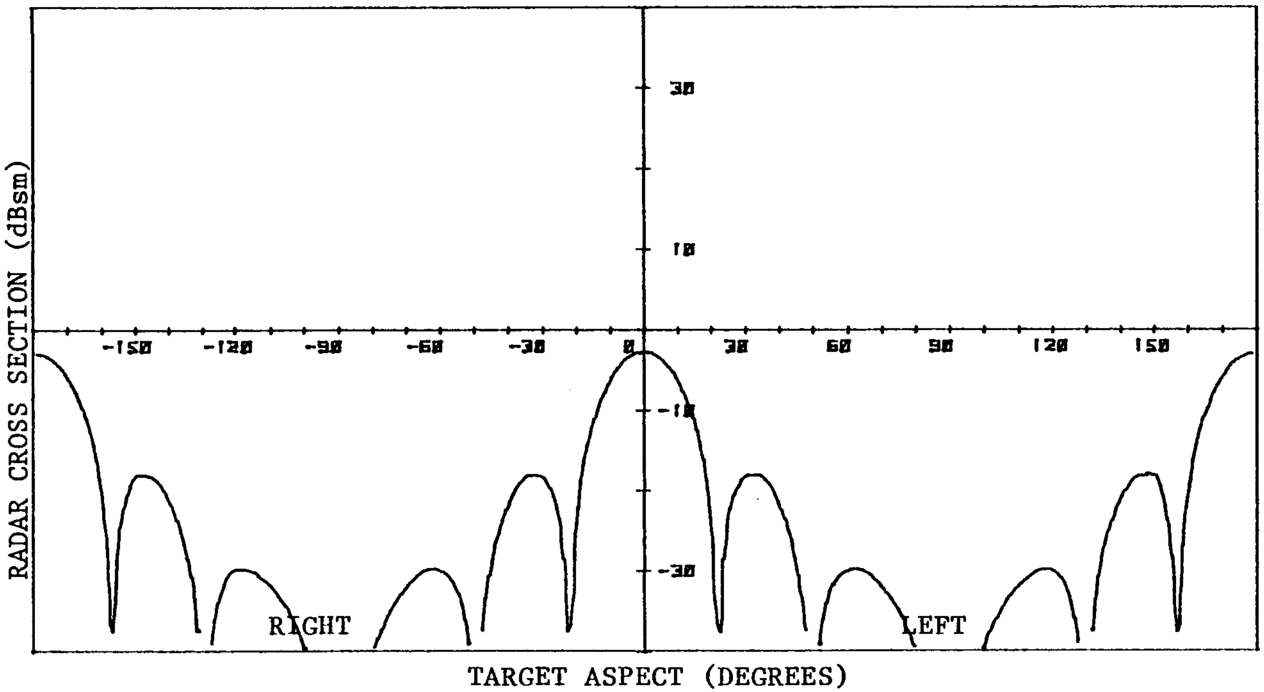

FIGURE 6.5

FIN SUPPORT WIRE RADAR CROSS SECTION

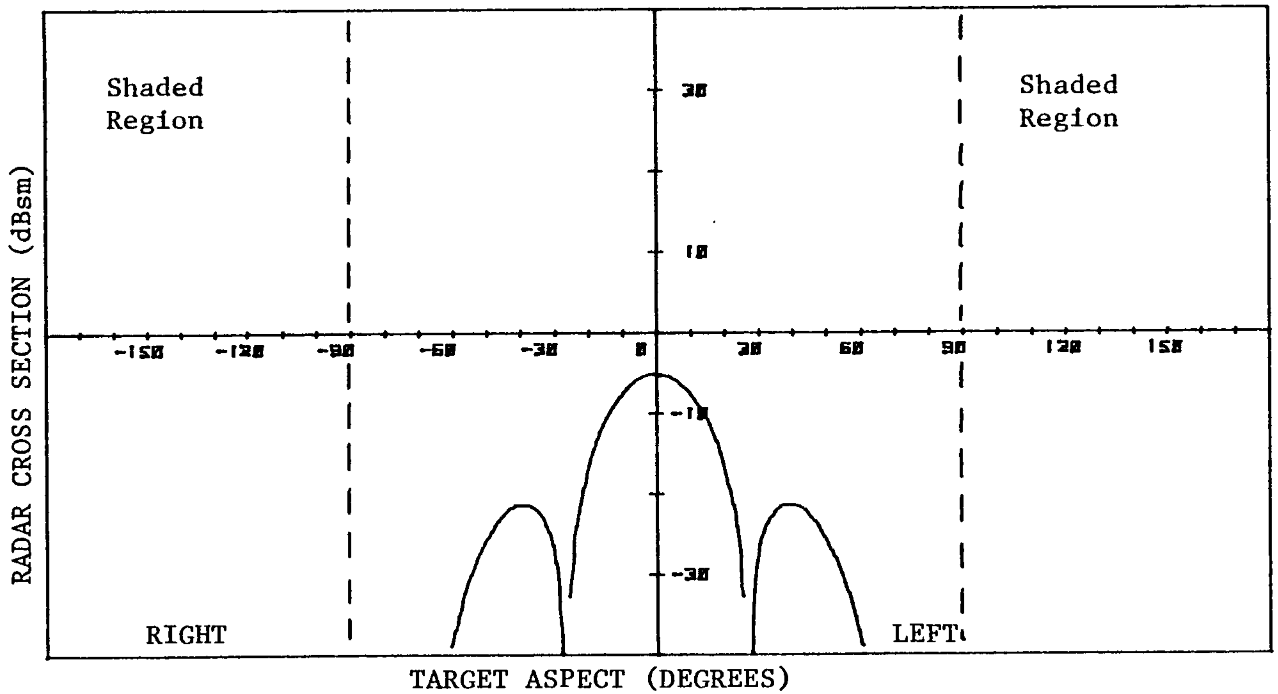

FIGURE 6.6

FRONT STRUT SUPPORT RADAR CROSS SECTION

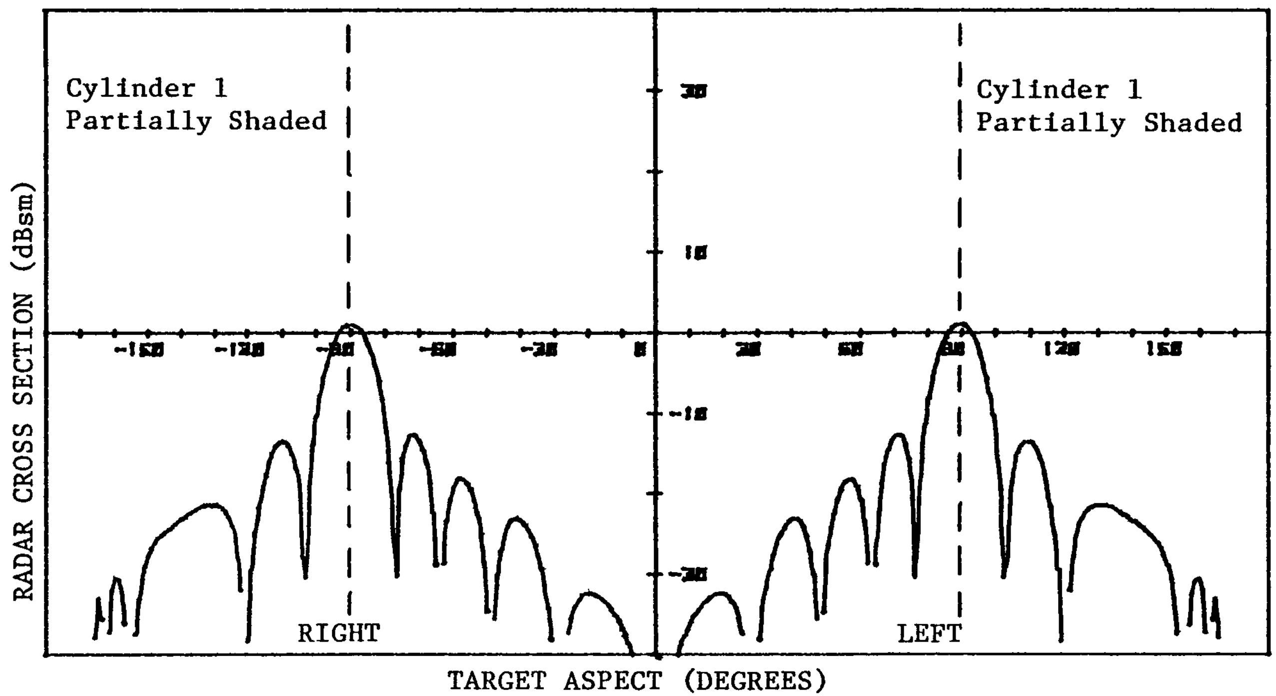

FIGURE 6.7

CYLINDER 1 RADAR CROSS SECTION

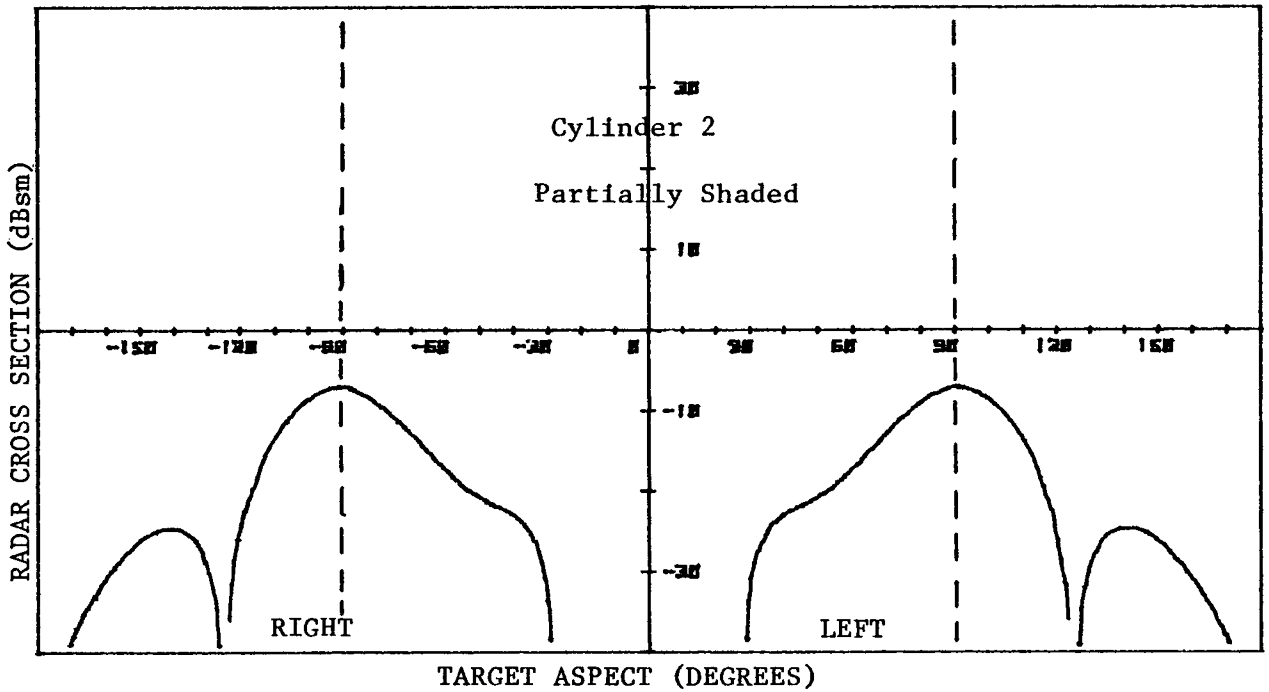

FIGURE 6.8

CYLINDER 2 RADAR CROSS SECTION

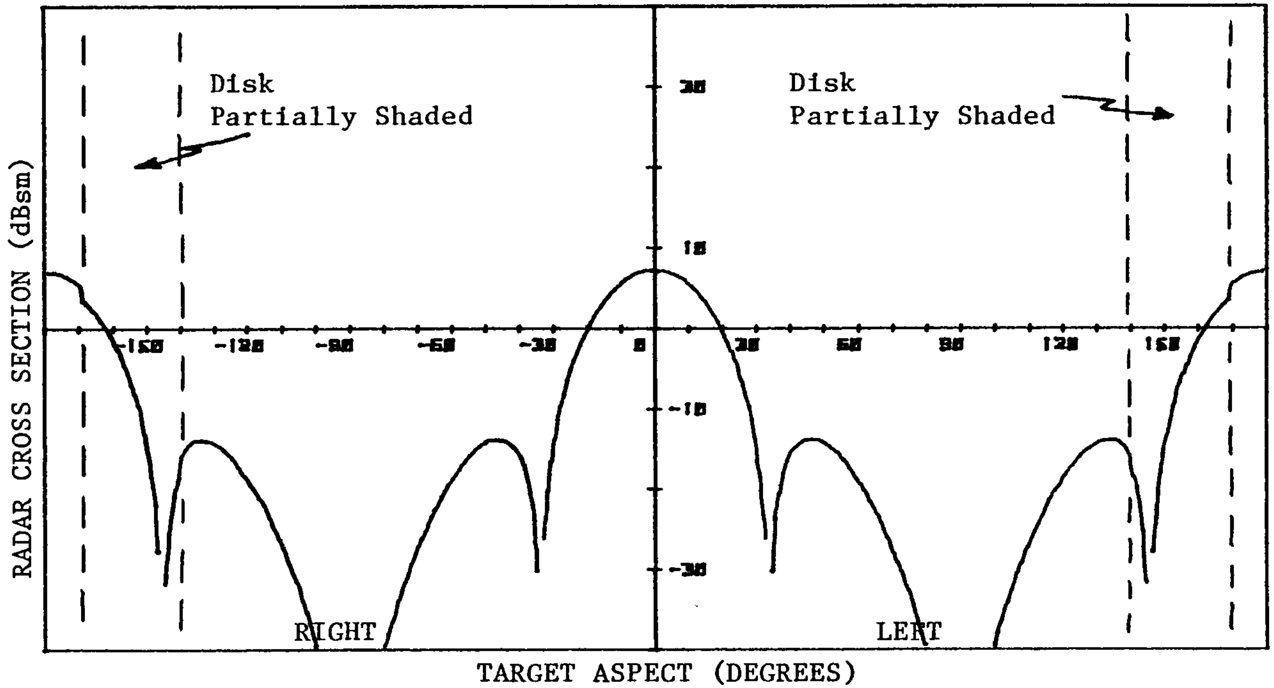

FIGURE 6.9

DISK RADAR CROSS SECTION

In conclusion, the results depicted in Figure 6.1 (p. 19) indicate that the model presented in this study will satisfy the goal of the Navy to develop a model to accurately estimate the RCS of the LOFAT in B-Band. In the most important regions of a target (nose, tail, and broadside) agreement between measured and calculated RCS of ± 2 dB was achieved. Computer listings of the composite model program are presented in the Appendix.

BIBLIOGRAPHY

BIBLIOGRAPHY

1. Skolnik, M. I. Introduction to Radar Systems. McGraw-Hill Book Company, New York, 1962.

2. Crispin, Jr., J. W., and K. M. Siegel. Methods of Radar Cross-Section Analysis. Academic Press, New York, 1968.

3. Keller, J. B. Geometrical Theory of Diffraction. Journal of the Optical Society of America, volume 52, number 2, pp. 116-130, February 1962.

4. Radar Cross Section Measurements of the LOFAT Tow Target in B-Band. Enclosure (1), letter serial number J-319, Pacific Missile Test Center, California, July 1977.

5. Crispin, Jr., J. W. and A. L. Moffett. Radar Cross Section Estimation for Simple Shapes. Proceedings of the IEEE, volume 53, number 8, pp. 833-847, August 1965.

6. Crispin, J. W., Jr., R. F. Goodrich and K. M. Siegel. A Theoretical Method for the Calculation of the Radar Cross Sections of Aircraft and Missiles. The University of Michigan, Ann Arbor, Report 2591-1-H, July 1959.

APPENDIX

COMPUTER LISTINGS

```
0: "COMPOSITE RADAR CROSS SECTION FOR 0 TO 90":
1: dim B[6],C[6],U[7],V[8],W[8]
2: "A=llambda=wavelength":
3: "B[N]=radii of component structures":
4: "C[N]=lengths of component structures":
5: "D=phi (in degrees)":
6: "G=variable from SIGMA routine":
7: "H=counter and theta":
8: "J=Bessel Function":
9: "R=variable from WIRE routine":
10: "S=Struve Function":
11: "U[N]=sigmas of component structures":
12: "V[N]=dNs of component structures":
13: "W[N]=theta Ns of component structures":
14: "Z=sigma of total composite structure":
15: prt "enter R and G "
16: spc 2
17: ent R,G
18: prt "enter llambda"
19: spc 2
20: ent A
21: prt "enter DISC      radius"
22: spc 2
23: ent B[1]
24: prt "enter CYLINDER  radius and      length"
25: spc 2
26: ent B[2],C[1]
27: prt "enter WIRE      radius, length, and phi"
28: spc 2
29: ent B[3],C[2],D
30: prt "enter PLATE     length and width"
31: spc 2
32: ent C[3],E
33: prt "enter CYLINDER 2radius"
34: spc 2
35: ent B[4]
36: prt "enter wire 3 length and radius"
37: spc 2
38: ent C[5],B[5]
39: prt "enter wire 4 length and radius"
40: spc 2
```

```
41: ent C[6],B[6]
42: scl -180,180,-40,40
43: csiz 1.5,1.3,.7,0
44: plt -170,35,1
45: lbl "COMBINATION 3"
46: plt -180,-40,1
47: iplt 360,0,2
48: iplt 0,80
49: iplt -360,0
50: iplt 0,-80,-1
51: axe 0,0,10,10
52: fxd 0
53: csiz 1.5,1.7,.7,0
54: -30→Y
55: plt 0,Y,1
56: cplt 1.3,-.3
57: lbl Y
58: Y+20→Y
59: if Y<=30;gto 55
60: csiz 1.5,1.7,.7,0
61: -150→X
62: plt X,0,1
63: cplt -2.5,-1.3
64: lbl X
65: X+30→X
66: if X<=150;gto 62
67: "* * * * * * * *":
68: for H=1 to 89
69: "DISC ROUTINE":
70: deg;4πB[1]sin(H)/A→I
71: gsb "BESSEL FUNCTION"
72: deg;J^2πB[1]^2/tan(H)^2→U[1];U[1]→U[1]
73: "CYLINDER 1 ROUTINE":
74: 4πB[2]sin(H)/A→I
75: gsb "STRUVE FUNCTION"
76: gsb "BESSEL FUNCTION"
77: deg;π(B[2]sin(H)/cos(H))^2→K
78: deg;2πC[1]cos(H)/A→L
79: rad;sin(L)→L;KL^2→K
80: 2/π-S→S
```

```
81: K(J^2+S^2)→U[3]
82: "FRONT STRUTS":
83: deg;πC[2]^2cos(H)^2→r1
84: deg;2πC[2]sin(H)/A→L
85: rad;(sin(L)/L)^2→r2
86: deg;Rcos(D)^4/3→r3
87: deg;(π/2)^2+ln(A/1.78πB[3]cos(H))^2→r4
88: r1*r2*r3/r4→U[2]
89: "FRONT STRUT SUPPORT":
90: deg;πC[5]^2cos(H)^2→r5
91: deg;2πC[5]sin(H)/A→r6
92: rad;(sin(r6)/r6)^2→r7
93: deg;(π/2)^2+ln(A/1.78πB[5]cos(H))^2→r8
94: 8*r5*r7/(3*r8)→U[6]
95: "FIN SUPPORT":
96: deg;πC[6]^2cos(H)^2→r9
97: deg;2πC[6]sin(H)/A→r10
98: rad;(sin(r10)/r10)^2→r11
99: deg;(π/2)^2+ln(A/1.78πB[6]cos(H))^2→r12
100: 8*r9*r11/(3*r12)→U[7]
101: "PLATE ROUTINE":
102: deg;π(2EC[3]sin(H)/A)^2→K
103: deg;2πC[3]cos(H)/A→L
104: rad;sin(L)→M
105: K(M/L)^2→U[4]
106: "CYLINDER 2 ROUTINE":
107: if H<=28;0→C[4];jmp 2
108: deg;.61-.32/tan(H)→C[4]
109: deg;4πB[4]sin(H)/A→I
110: gsb "STRUVE FUNCTION"
111: gsb "BESSEL FUNCTION"
112: deg;π(B[4]sin(H)/cos(H))^2→K
113: deg;2πC[4]cos(H)/A→L
114: rad;sin(L)→L;KL^2→K
115: 2/π-S→S
116: K(J^2+S^2)→U[5]
117: "SIGMA ROUTINE":
118: 0→V[1]
119: deg;if H<=11;-Gsin(79+H)→V[2];jmp 2
120: deg;-Gsin(101-H)→V[2]
```

```
121: deg;if H<=79;-Gsin(79-H)→V[3];jmp 2
122: deg;Gsin(H-79)→V[3]
123: deg;-.8cos(H)→V[4]
124: deg;if H<=52;.8sin(52-H)→V[5];jmp 2
125: deg;-.8sin(H-52)→V[5]
126: if H<=28;0→V[6];jmp 2
127: deg;(.31+.15/tan(H))cos(H)→V[6]
128: deg;-1.55cos(H)→V[7]
129: deg;1.15cos(H)→V[8]
130: for N=1 to 8
131: 4πV[N]/A→W[N]
132: next N
133: rad;√U[1]+√U[2](cos(W[2])+cos(W[3]))+√U[3]cos(W[4])→X
134: rad;X+√U[4]cos(W[5])+√U[5]cos(W[6])→X
135: rad;X+√U[6]cos(W[7])+√U[7]cos(W[8])→X
136: rad;√U[2]*(sin(W[2])+sin(W[3]))+√U[3]sin(W[4])→Y
137: rad;Y+√U[4]sin(W[5])+√U[5]sin(W[6])→Y
138: rad;Y+√U[6]sin(W[7])+√U[7]sin(W[8])→Y
139: X^2+Y^2→Z
140: 10log(Z)→Z
141: Z→r(H+20)
142: next H
143: for H=1 to 85
144: (r(H+20)+r(H+21)+r(H+22)+r(H+23)+r(H+24))/5→Z
145: plt H+2,Z
146: next H
147: "STRUVE FUNCTION":
148: I^2/4→Q
149: √π→L;0→O;.5√π→P
150: for T=0 to 9
151: (-1)^T*(I/2)^(2T)→K
152: (T+.5)L→L
153: (T+1.5)P→P
154: K/LP+O→O
155: next T
156: QO→S
157: ret
158: "BESSEL FUNCTION":
159: 0→N
160: (I/2)^(2N+1)(-1)^N→K
```

```
161: N→M
162: 1→L→O
163: 1→P
164: if M=0;gto 168
165: if M-1=0;gto 168
166: PM→P
167: M-1→M;gto 165
168: PL→L
169: if O=1;N+1→M;M+1→O;gto 163
170: K/L→rN;N-1→Q
171: if N>0;rN+rQ→rN
172: if N=11;rN→J;jmp 2
173: N+1→N;gto 160
174: ret
175: end
```

```
0: "COMPOSITE RADAR CROSS SECTION FOR 90 TO 180":
1: dim B[6],C[6],U[6],V[7],W[7]
2: "A=llambda=wavelength":
3: "B[N]=radii of component structures":
4: "C[N]=lengths of component structures":
5: "D=phi (in degrees)":
6: "G=variable from SIGMA routine":
7: "H=counter and theta":
8: "J=Bessel Function":
9: "R=variable from WIRE routine":
10: "S=Struve Function":
11: "U[N]=sigmas of component structures":
12: "V[N]=dNs of component structures":
13: "W[N]=theta Ns of component structures":
14: "Z=sigma of total composite structure":
15: prt "enter R and G "
16: spc 2
17: ent R,G
18: prt "enter llambda"
19: spc 2
20: ent A
21: prt "enter DISC      radius"
22: spc 2
23: ent B[1]
24: prt "enter CYLINDER  radius and      length"
25: spc 2
26: ent B[2],C[1]
27: prt "enter WIRE      radius, length, and phi"
28: spc 2
29: ent B[3],C[2],D
30: prt "enter PLATE     length and width"
31: spc 2
32: ent C[3],E
33: prt "enter CYLINDER 2radius and length"
34: spc 2
35: ent B[4],C[4]
36: prt "ENTER WIRE 4  LENGTH & RADIUS"
37: spc 2
38: ent C[6],B[6]
```

```
39: scl -180,180,-40,40
40: csiz 1.5,1.3,.7,0
41: plt -170,35,1
42: lbl "COMBINATION 3"
43: plt -180,-40,1
44: iplt 360,0,2
45: iplt 0,80
46: iplt -360,0
47: iplt 0,-80,-1
48: axe 0,0,10,10
49: fxd 0
50: csiz 1.5,1.7,.7,0
51: -30→Y
52: plt 0,Y,1
53: cplt 1.3,-.3
54: lbl Y
55: Y+20→Y
56: if Y<=30;gto 52
57: csiz 1.5,1.7,.7,0
58: -150→X
59: plt X,0,1
60: cplt -2.5,-1.3
61: lbl X
62: X+30→X
63: if X<=150;gto 59
64: "* * * * * * * *":
65: for H=91 to 179
66: "DISC ROUTINE":
67: deg;4πB[1]sin(H)/A→I
68: gsb "BESSEL FUNCTION"
69: deg;J^2πB[1]^2/tan(H)^2→U[1]
70: U[1]→U[1]
71: if H<=140;jmp 3
72: if H>=170;jmp 2
73: .7U[1]→U[1]
74: "CYLINDER 1 ROUTINE":
75: deg;4πB[2]sin(H)/A→I
76: gsb "STRUVE FUNCTION"
77: gsb "BESSEL FUNCTION"
78: deg;π(B[2]sin(H)/cos(H))^2→K
79: deg;-2π(C[1]-.38tan(H-90))cos(H)/A→L
80: rad;sin(L)→L;KL^2→K
```

```
81: 2/π-S→S
82: if H<=166;K(J^2+S^2)→U[3];jmp 2
83: 0→U[3]
84: "FRONT STRUTS":
85: deg;πC[2]^2cos(H)^2→r1
86: deg;2πC[2]sin(H)/A→L
87: rad;(sin(L)/L)^2→r2
88: deg;Rcos(D)^4/3→r3
89: deg;(π/2)^2+ln(A/-1.78πB[3]cos(H))^2→r4
90: r1*r2*r3/r4→U[2]
91: "FIN SUPPORT":
92: deg;πC[6]^2cos(H)^2→r9
93: deg;2πC[6]sin(H)/A→r10
94: rad;(sin(r10)/r10)^2→r11
95: deg;(π/2)^2+ln(A/-1.78πB[6]cos(H))^2→r12
96: 8*r9*r11/(3*r12)→U[6]
97: "PLATE ROUTINE":
98: deg;π(2EC[3]sin(H)/A)^2→K
99: deg;-2πC[3]cos(H)/A→L
100: rad;sin(L)→M
101: K(M/L)^2→U[4];6U[4]→U[4]
102: "CYLINDER 2 ROUTINE":
103: deg;4πB[4]sin(H)/A→I
104: gsb "STRUVE FUNCTION"
105: gsb "BESSEL FUNCTION"
106: deg;π(B[4]sin(H)/cos(H))^2→K
107: deg;-2πC[4]cos(H)/A→L
108: rad;sin(L)→L;KL^2→K
109: 2/π-S→S
110: K(J^2+S^2)→U[5]
111: "SIGMA ROUTINE":
112: 0→V[1]
113: deg;if H<=173;1.56sin(H-83)→V[2];jmp 2
114: deg;1.56cos(H-173)→V[2]
115: deg;if H<=97;-1.56sin(97-H)→V[3];jmp 2
116: deg;1.56sin(H-97)→V[3]
117: deg;if H<=166;(.8+.19tan(H-90))sin(H-90)→V[4]
118: deg;if H<=142;-.8sin(H-52)→V[5];jmp 2
119: deg;-.8cos(H-142)→V[5]
120: deg;-(C[4]/2)sin(H-90)→V[6]
```

```
121: deg;1.19cos(H)→V[7]
122: for N=1 to 7
123: 4πV[N]/A→W[N]
124: next N
125: rad;√U[1]+√U[2](cos(W[2])+cos(W[3]))+√U[3]cos(W[4])→X
126: rad;X+√U[4]cos(W[5])+√U[5]cos(W[6])→X
127: X+√U[6]cos(W[7])→X
128: rad;√U[2]*(sin(W[2])+sin(W[3]))+√U[3]sin(W[4])→Y
129: rad;Y+√U[4]sin(W[5])+√U[5]sin(W[6])→Y
130: Y+√U[6]sin(W[7])→Y
131: X^2+Y^2→Z
132: 10log(Z)→Z
133: Z→rH
134: next H
135: for H=91 to 175
136: (r(H+1)+r(H+2)+r(H+3)+r(H+4)+rH)/5→Z
137: plt H+2,Z
138: next H
139: "STRUVE FUNCTION":
140: I^2/4→Q
141: √π→L;0→O;.5√π→P
142: for T=0 to 9
143: (-1)^T*(I/2)^(2T)→K
144: (T+.5)L→L
145: (T+1.5)P→P
146: K/LP+O→O
147: next T
148: QO→S
149: ret
150: "BESSEL FUNCTION":
151: 0→N
152: (I/2)^(2N+1)(-1)^N→K
153: N→M
154: 1→L→O
155: 1→P
156: if M=0;gto 160
157: if M-1=0;gto 160
158: PM→P
159: M-1→M;gto 157
160: PL→L
```

```
161: if O=1;N+1→M;M+1→O;gto 155
162: K/L→rN;N-1→Q
163: if N>0;rN+rQ→rN
164: if N=11;rN→J;jmp 2
165: N+1→N;gto 152
166: ret
167: end
```

VITA

Lawrence P. Talley was born in Miami, Florida on August 11, 1945. Following his graduation from LaPlata High School, LaPlata, Maryland, he entered a work-study program with the Department of Navy and the University of Maryland. He was awarded the degree of Bachelor of Science in Electrical Engineering in June 1968.

After graduating from the University of Maryland, he entered full-time employment at the Naval Air Test Center, Patuxent River, Maryland, where he is presently employed. Since his employment, he has evaluated radar systems on F-8, F-4, F-14 and E-2 airplanes. Mr. Talley was awarded the John E. Burdette Memorial Award as the outstanding project engineer at the Naval Air Test Center in 1977.

He is married to the former Janice A. Tilley of Maryville, Tennessee.